PCCP

PAPER

View Article Online
View Journal | View Issue

Cite this: *Phys. Chem. Chem. Phys.*, 2017, **19**, 673

Reversible ultrafast spin switching on Ni@B_{80} endohedral fullerene

Chun Li,*[a] Jing Liu,[a] Georgios Lefkidis[ab] and Wolfgang Hübner[b]

Received 21st September 2016,
Accepted 21st November 2016

DOI: 10.1039/c6cp06492b

www.rsc.org/pccp

We present the configurations and stability of the endohedral metallofullerene Ni@B_{80} by using strict and elaborate geometric modeling. The ultrafast spin switching on Ni@B_{80} is explored through *ab initio* calculations. It is shown that there are three stable configurations of Ni@B_{80} endohedral fullerene with the encaged Ni atom located at different sites. The ultrafast spin switching on Ni@B_{80} *via* Λ processes can be achieved through at least eight paths with different laser pulses. Among them, the fastest one can be accomplished within 100 fs. In particular, it is found that all the spin-switching processes achieved on the H-type structure are reversible with the use of the same or different laser pulses. Considering the obtained high fidelities of these switching processes, the present theoretical prediction could lead to promising applications in the design of integrated spin-logic devices through appropriate spin manipulation in endohedral boron fullerenes.

1 Introduction

In recent years, ultrafast spin dynamics on magnetic nanostructures has become an increasingly intensive research field in order to develop novel spin devices serving as a substitute for traditional electronic ones by manipulating the spin degree of freedom of specific systems. Since Bigot and his co-workers first discovered ultrafast magnetization in ferromagnetic metals in 1996,[1] the ultrafast spin dynamics has made remarkable progress and has become relevant for a wide range of research areas and applications involving bulk materials, thin films, nanostructures, and molecular magnets in the past ten years.[2–8]

As is typical for fullerene-based materials, endohedral fullerenes are characterized by a robust fullerene cage with atoms, ions, or clusters trapped in its hollow. Because of the electron transfer from the encaged species to the fullerene cage, such molecules open many possibilities for applications and have therefore been attracting wide interest in interdisciplinary research areas.[9–13] Endohedral fullerenes can be conducive to spin manipulation because the fullerene cage can serve as a sheltering room for the inner spin system which prevents the desired dynamics from being disturbed by the external environment.[14,15] In addition, the robustness of the structure and long coherence time of the electronic states give to these compounds great potential to serve as functional information carriers in future nano-spintronics applications.[16] These excellent characteristics have drawn wide attention of scientists and given new impetus to the efforts toward the practical application and theoretical investigation of endohedral fullerenes. Harneit *et al.* explored the possibilities of using endohedral fullerenes N@C_{60} and P@C_{60} as quantum-information carriers.[17] Ju *et al.* proposed a new scalable quantum computer architecture based on the nuclear spin manipulation on endohedral fullerene molecules.[18] Li *et al.* proposed a theory for manipulating the spin degree of freedom in Co_2C_{60}.[19,20] These investigations provide the background for designing fullerene-based spin-logic devices and also stimulate further theoretical and experimental studies in order to explore controllable ultrafast spin manipulations.

However, up to now most researchers have focused on the properties and applications of carbon fullerenes, while for a long time non-carbon fullerenes have drawn much less attention, due to the difficulties in their experimental synthesis. After Gonzalez *et al.* predicted a stable atomic arrangement of the fullerene B_{80} in 2007,[21] boron fullerenes began to attract scientists' interest. B_{80} is believed to be a large soccer-like molecule with a wide hollow space inside (although a recent study using minimal-hopping global-geometry optimization predicts a multitude of stable structures[22]). The boron cage consists of 20 hexagons and 12 pentagons, and is structurally similar to C_{60} except that there are 20 additional boron atoms lying on the sites near the center of the hexagons.[23–28] The quite large energy gap (almost 1 eV) between the highest occupied molecular orbital (HOMO) and the lowest unoccupied molecular orbital (LUMO) also furnishes a proof of the stability of B_{80}.[23,24,27] Because of this and its C_{60}-like structure, scientists have also been motivated to find new stable configurations of endohedral

[a] *School of Mechanics, Civil Engineering and Architecture, Northwestern Polytechnical University, Xi'an 710072, China. E-mail: lichun@nwpu.edu.cn*
[b] *Department of Physics and Research Center OPTIMAS, University of Kaiserslautern, P. O. Box 3049, 67653 Kaiserslautern, Germany*

B_{80} fullerenes. Recently, Wang *et al.* explored the structural stability of boron caged $B@Co_{12}@B_n$ and $Co_{13}@B_n$ clusters, and showed the desirable properties of $B@Co_{12}@B_{80}$, such as the large binding energy of the closed-shell electronic structure.[24] Li *et al.* presented the geometric and magnetic properties of three stable configurations of $Ni@B_{80}$ and $Fe@B_{80}$.[25,26] Interestingly, according to the investigation of Bean *et al.*, the quite large and positive NICS (nucleus independent chemical shift) value suggests magnetic deshielding at various extra-nuclear points inside the B_{80} cages, which is opposite to the inner space of C_{60} cages.[29] This property indicates the spin manipulation on inner magnetic atoms of endohedral boron fullerenes by applying an external magnetic field. Experimentally, several endohedral boron fullerenes have already been synthesized[30,31] and their stability has also been investigated.[32,33] In addition, there are other theoretical groups investigating the newly established field of endohedral boron-fullerenes.[34–36] However, to the best of our knowledge, the study of the spin dynamics in endohedral boron fullerenes, which is indispensable before exploiting them in future nano-spintronic devices, has not been reported yet.

In this paper, the laser-induced ultrafast spin-switching mechanism of $Ni@B_{80}$ is systematically investigated by combining high-level *ab initio* calculations with the well-developed theoretical framework of spin-switching Λ processes. The geometry and the spin density distribution of the system are also studied in depth. Three stable configurations of $Ni@B_{80}$ are found, which can be identified by the location of the Ni atoms in the boron cage. In addition, several subpicosecond spin-switching scenarios on $Ni@B_{80}$ are proposed, with the fastest one completing within only 100 fs. It is noteworthy, that some of the spin switching scenarios can be achieved with more than one set of laser parameters, thus rendering them experimentally easier to realize.

2 Modeling and technique details

2.1 Structure construction and optimization

In order to properly describe the spin-dynamics behavior of $Ni@B_{80}$ endohedral fullerene, we first have to determine the geometry of $Ni@B_{80}$. $Ni@B_{80}$ can be divided into three parts: a C_{60}-like cluster B_{60}, additional 20 boron atoms located near the center of hexagons, and an isolated Ni atom. The model of B_{60} is built firstly referring to the geometry modelling of C_{60}.[37] The built B_{60} forms the basic frame of the whole fullerene molecule and plots out the initial areas for the other atoms. Due to their geometric similarity we hypothesize that both C_{60} and B_{80} have the same icosahedral symmetry (point group I_h). The structure can be formed by equally removing 12 vertices of the regular icosahedron. As shown in Fig. 1(a), vertex F is sitting on the z axis, which is also the 5-fold axis of the icosahedron. The coordinates of point F are $(0,0,R)$. Point A is located on the plane xoz, a mirror plane of the icosahedron. Therefore, the coordinates of point A are assumed to be $(a,0,c)$. Since both F and A are on the surface of the circumscribed sphere of the regular icosahedron, it is easy to demonstrate that $R = \sqrt{a^2 + c^2}$.

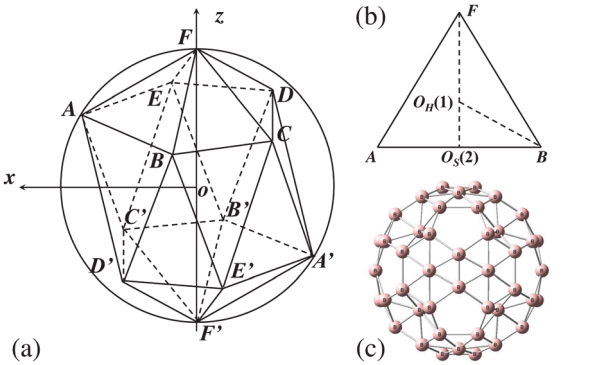

Fig. 1 (a) Regular icosahedron and its circumscribed sphere. (b) The location of the center of a hexagon, where $O_S(2)$ is the midpoint of line AB, and $O_H(1)$ denotes the centroid of ΔABF (also the center of a hexagon). (c) The relaxed configuration of B_{80}.

The coordinates of points B, C, D, and F, can be obtained by $\frac{2\pi}{5}$ rotations of point A around the z axis. The respective position vectors are

$$\begin{aligned}
\overrightarrow{oA} &= a\vec{i} + 0\vec{j} + c\vec{k},\\
\overrightarrow{oB} &= a\cos 72^\circ \vec{i} + a\sin 72^\circ \vec{j} + c\vec{k},\\
\overrightarrow{oC} &= a\cos 144^\circ \vec{i} + a\sin 144^\circ \vec{j} + c\vec{k},\\
\overrightarrow{oD} &= a\cos 216^\circ \vec{i} + a\sin 216^\circ \vec{j} + c\vec{k},\\
\overrightarrow{oE} &= a\cos 288^\circ \vec{i} + a\sin 288^\circ \vec{j} + c\vec{k}.
\end{aligned} \tag{1}$$

In order to calculate the 60 coordinates of each boron atoms of the B_{60} cluster, 20 identical pentagonal pyramids are removed from the vertices of the icosahedron, and a new parameter λ is defined as the ratio of the intercepted length to the initial length of the edge. For example, there will be two additional points $b_1(1)$ and $b_2(1)$ on the line AF, after removing the two pentagonal pyramids corresponding to points A and F. In other words, $b_1(1)$ and $b_2(1)$ are the positions of two boron atoms of a B_{60} cluster, and their position vectors can be expressed as

$$\begin{aligned}
\overrightarrow{ob_1(1)} &= \overrightarrow{oF} + \lambda\left(\overrightarrow{oA} - \overrightarrow{oF}\right)\\
&= \lambda a\vec{i} + 0\vec{j} + [\lambda c + (1 - \lambda R)]\vec{k},
\end{aligned} \tag{2}$$

$$\begin{aligned}
\overrightarrow{ob_2(1)} &= \overrightarrow{oA} + \lambda\left(\overrightarrow{oF} - \overrightarrow{oA}\right)\\
&= (1 - \lambda)a\vec{i} + 0\vec{j} + [(1 - \lambda)c + \lambda R]\vec{k}.
\end{aligned} \tag{3}$$

The coordinates of the other four points on B_{60}, $b_3(1)$ and $b_4(1)$ on line AB, $b_5(1)$ on line AD' and $b_6(1)$ on line BD', are be obtained in a similar manner. The positions of the rest points can be located through appropriate symmetry operations of the

following basis: (i) $\frac{2\pi}{5}$ rotation around the z axis, and (ii) inversion through the origin o.

The three unknown constants a, c and λ, with the value of the known bond length and the mathematical relationship between the known parameters and the unknowns, can be found from the following equations:

$$L_{\mathrm{HH}} = \left|\overrightarrow{ob_1(1)} - \overrightarrow{ob_2(1)}\right| = 1.70\ \text{Å} \quad (4)$$

$$L_{\mathrm{HP}} = \left|\overrightarrow{ob_1(1)} - \overrightarrow{ob_1(2)}\right| = 1.74\ \text{Å} \quad (5)$$

$$a = \frac{\sqrt{1-2\cos 72^\circ}}{1-\cos 72^\circ} \quad (6)$$

$$c = \frac{R\cos 72^\circ}{1-\cos 72^\circ} \quad (7)$$

For the additional 20 boron atoms sitting on the sites close to the centers of hexagons, we first assume that there are no irregularities on the surface of the boron cage, and that these atoms are located exactly at the centers of the hexagons. Therefore, the initial coordinates of boron atoms directly correspond to the coordinates of the centers of the hexagons (obviously the centers of the hexagons are also the centroids of the 20 triangular faces of the icosahedron). To locate these additional boron atoms, we take the centroid of ΔABF named $O_{\mathrm{H}}(1)$ as a basis, as shown in Fig. 1(b), and write its position vector as follows:

$$\overrightarrow{oO_{\mathrm{H}}(1)} = \left[\overrightarrow{oF} - \overrightarrow{oO_{\mathrm{S}}(2)}\right] \times \frac{1}{3} + \overrightarrow{oO_{\mathrm{S}}(2)}. \quad (8)$$

The centroid of $\Delta ABD'$, referred to as $O_{\mathrm{H}}(2)$, cannot be reached by any symmetry operations of $O_{\mathrm{H}}(1)$, therefore this point is also part of the basis. Using the coordinates of points A, B, and D', the position vector of $O_{\mathrm{H}}(2)$ can be expressed as

$$\overrightarrow{oO_{\mathrm{H}}(2)} = \left[\overrightarrow{oD'} - \overrightarrow{oO_{\mathrm{S}}(2)}\right] \times \frac{1}{3} + \overrightarrow{oO_{\mathrm{S}}(2)}. \quad (9)$$

Through the previously mentioned symmetry operations, the coordinates of the remaining 18 boron atoms can be easily calculated as well. Fig. 1(c) depicts the starting, perfectly symmetric geometry constructed with these considerations.

We optimize the starting geometry of B_{80} using the Gaussian 09 package[38] with the restricted open shell Hartree–Fock (ROHF) method (in order to avoid spin contamination). We employ four geometry convergence criteria: (i) the maximum component of the force must be below the cutoff value of 4.5×10^{-4} Hartree Bohr^{-1}, (ii) the root-mean-square of the forces must be below 3.0×10^{-4} Hartree Bohr^{-1}, (iii) the calculated displacement for the next step must be kept below 1.8×10^{-3} Bohr, and (iv) the root-mean-square of the displacement for the next step must be smaller than the cutoff value of 1.2×10^{-3}. Finally, we place the Ni atom into the inner hollow area of the optimized B_{80} cage and re-optimize the whole structure. The stability of the final optimized geometry is verified by the absence of imaginary normal-mode frequencies.

2.2 Computational method for spin switching

In the past, we have presented several ultrafast laser-induced magnetization-dynamics scenarios on various bare as well as ligand-stabilized molecular systems.[39–43] In particular, by taking advantage of suitable Λ processes one can realize four different scenarios: (1) (partial) demagnetization, (2) spin switching, (3) spin transfer, and (4) simultaneous spin switching and spin transfer.[44] The improved processes proposed in the manuscript are also based on optical transitions and driven by a coherent laser field between the ground states (initial and final states) and other well-defined electronic excited states (intermediate states) of our magnetic system.

The one-electron wave functions are obtained with the Hartree–Fock method using the STO-3G basis set for the B atoms and the Los Alamos basis set (LanL2DZ)[45] plus double ζ with relativistic effective core potentials (ECP) for the Ni atom (these basis sets have proven successful on numerous strongly correlated materials and endohedral fullerene systems before[19,20,41,46]). This is also the level at which we perform the geometry optimization. Then, the electronic correlations are included by the symmetry-adapted-cluster configuration-interaction (SAC-CI) method[47] and the many-body electron wave functions are obtained, as implemented in the Gaussian 09 package.[38] In order to achieve high numerical accuracy at a realistic computational cost, we repeat the SAC-CI calculations twice. The first time, in which we allow only for singles virtual excitations, is used to deduce the necessary active window. This window comprises 196 molecular orbitals and is capable of accounting for the correlated d–d transitions of the Ni atom. The second time we allow up to quadruple one-electron virtual excitations.

Subsequently, we perturbatively include spin–orbit coupling (SOC) and a static external magnetic field along the z direction ($B_{\mathrm{stat.}} = 10^{-5}$ at. un. = 2.35 T) in order to obtain the Zeeman splitting and the necessary spin-mixed states.[41,43] The corresponding Hamiltonian is

$$\hat{H}^{(1)} = \sum_{i=1}^{n} \frac{Z_{\mathrm{a}}^{\mathrm{eff}}}{2c^2 R_i^3}\hat{\mathbf{L}}\cdot\hat{\mathbf{S}} + \sum_{i=1}^{n}\mu_{\mathrm{L}}\hat{\mathbf{L}}\cdot\mathbf{B}_{\mathrm{stat.}} + \sum_{i=1}^{n}\mu_{\mathrm{S}}\hat{\mathbf{S}}\cdot\mathbf{B}_{\mathrm{stat.}} \quad (10)$$

$Z_{\mathrm{a}}^{\mathrm{eff}}$ denotes the relativistic effective nuclear charges which are used for the SOC. $\hat{\mathbf{L}}$ and $\hat{\mathbf{S}}$ are the orbital and spin momentum operators, respectively. μ_{L} and μ_{S} are their respective gyromagnetic ratios, and c is the speed of light. After including the SOC and the external magnetic field, the transition matrix elements of the electric-dipole-transition operator $\hat{\mathbf{D}}$ and the spin momentum operator $\hat{\mathbf{S}}$ are calculated for every many-body-state pair. Finally, by using time-dependent perturbation theory, the wave function is propagated in time under the influence of a suitably tailored laser pulse with a simple sech^2-shaped envelope. The interaction between the aforementioned transition matrix and the laser pulse gives the time-dependent perturbation term in the Hamiltonian.

The propagation of the many-body wave functions can be described as the following equation,

$$\frac{\partial c_n}{\partial t} = -\frac{i}{\hbar}\sum_k \langle n|\hat{H}^{(2)}|k\rangle c_k(t) e^{-i(E_k-E_n)t/\hbar}, \qquad (11)$$

where $\hat{H}^{(2)}(t) = \mathbf{p}^{(1)}\cdot\mathbf{A}_{\text{laser}}(t) + \mathbf{S}\cdot\mathbf{B}_{\text{laser}}(t)$ is the Hamiltonian expressing the effect of the time-dependent laser pulse. $\mathbf{p}^{(1)}$, $\mathbf{A}_{\text{laser}}(t)$ and $\mathbf{B}_{\text{laser}}(t)$ are the electron momentum, the time-dependent vector potential and magnetic fields of the laser pulse, respectively. $\langle n|$ and $|k\rangle$ are the unperturbed eigenstates, c_n is the complex scalar coefficient of state k in the wave function $\psi(t) = \sum_n c_n e^{-iE_n t/\hbar}|n\rangle$, and E_n and E_k are the energies of states n and k, respectively. In order to solve the system of these partial differential equations, we implement our own codes, which use an embedded fifth-order Runge–Kutta method in combination with the Cash–Karp adaptive step-size control. This way, the complete time evolution of the Λ process can be obtained. The optimization of laser parameters is performed using a specially developed genetic algorithm.[48]

3 Results and discussions

3.1 Structural analysis

The optimization yields three stable geometries for Ni@B_{80} (Fig. 2): (i) the Ni atom sits near the center of a hexagon (H type); (ii) the Ni atom sits near the vertex of a pentagon (Pv type); (iii) the Ni atom sits near the midpoint of the B–B bond between two opposite hexagons (HH type). As discussed previously, the B–B bonds can be divided into three groups: 60 between pentagons and hexagons (L_{HP}), 30 between two neighboring hexagons (L_{HH}), and 120 between the atoms at the center of each hexagon and their nearest neighbors (L_{BB}).[25] The average bond lengths of the three groups in the present study (1.74, 1.63, and 1.73 Å, respectively) are similar to the previous density-functional calculations (1.74, 1.70, and 1.73 Å, respectively[25]). The distances between the Ni atom and the center of the boron cage are 1.747 Å (H type), 1.771 Å (Pv type) and 2.113 Å (HH type), respectively. Each structure exhibits a slight Jahn–Teller distortion in the vicinity of the Ni atom.

Note that out of the 20 additional boron atoms initially positioned in the center of the hexagons of B_{60}, 8 move inward and 12 move outward, and thus the final symmetry of B_{80} is reduced to T_{h} [Fig. 1(c)].

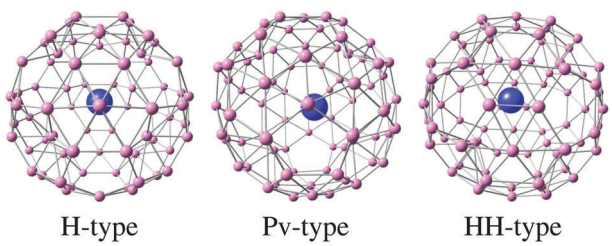

Fig. 2 Three optimized configurations of endohedral metallofullerene Ni@B_{80}. The red spheres denote boron atoms and the blue ones represent the Ni atom.

Table 1 The total energy and binding energy for three relaxed configurations of Ni@B_{80}

Type	E_{Ni} (eV)	$E_{B_{80}}$ (eV)	$E_{\text{tot.}}$ (eV)	$E_{\text{bind.}}$ (eV)
H			−57573.589	3.414
HH	−4577.34	−52992.835	−57573.347	3.172
Pv			−57570.175	1.179

In order to further ascertain the stability of the optimized geometries, we also look into the total binding energy of Ni@B_{80}, given as $E_{\text{bind.}} = E_{B_{80}} + E_{\text{Ni}} - E_{\text{tot.}}$, where $E_{B_{80}}$, E_{Ni}, and $E_{\text{tot.}}$ are the total energies of the isolated B_{80}, an isolated Ni atom, and the endohedral metallofullerene Ni@B_{80}, respectively (Table 1). In the rest of the manuscript we discuss the H-type configuration, which has the largest binding energy. In addition, we calculate the HOMO–LUMO energy gap of the magnetic system by applying HF and SAC-CI methods. The quite large resulting value (2.465 eV) also explains the stability of Ni@B_{80}. In addition, Fig. 3 shows the HOMO and LUMO of Ni@B_{80} as they are obtained from the Hartree–Fock calculations. According to our SAC-CI calculations, the LUMO makes a major contribution to the vast majority of the virtual excitations which constitute the correlations in the many-body wavefunctions. This results in a very strong interaction between the cage and the central Ni atom, which clearly explains the connection between spin localization and geometry.

3.2 Spin-switching processes on Ni@B_{80}

The spin density (calculated using Mulliken population analysis) reveals that, as anticipated, the greatest part of the spin density of the energetically lowest triplet states is localized on the enclosed Ni atom (Table 2). This is a necessary condition in order to exploit Ni@B_{80} for spin manipulation. Furthermore, the degree of spin localization of the triplet ground state is higher in the most stable geometry (H type), while the boron cage has

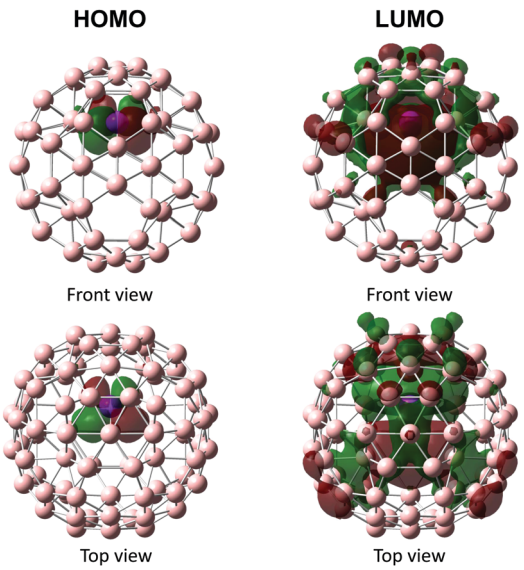

Fig. 3 The HOMO and LUMO of Ni@B_{80}. The isosurfaces of the wavefunctions are red and green for positive and negative values, respectively. The isovalue is 0.02.

Table 2 Spin density of the lowest five triplet states in Ni@B_{80} for the three different geometries. B(max) refers to the boron atom with the highest spin density

Type	Atom	State 1	State 2	State 3	State 4	State 5
H	Ni	1.591	0.982	0.983	0.978	0.963
	B(max)	0.021	0.056	0.059	0.064	0.043
HH	Ni	0.983	0.983	1.101	1.037	0.989
	B(max)	0.191	0.171	0.090	0.060	0.096
Pv	Ni	1.110	0.949	0.942	0.934	0.890
	B(max)	0.230	0.120	0.108	0.171	0.165

the lowest spin polarization (in other words, the spin density of the cage is almost equally distributed among the boron atoms). These observations further corroborate our choice of the H-type geometry as the best candidate for spin-manipulation.

To achieve Λ-process-based spin-switching on the H-type Ni@B_{80}, we need two ground states as the initial and final states, and some spin-mixed intermediate state(s). In particular, an initial intermediate state needs to be chosen first as an initial condition for the genetic algorithm. Previous theoretical work has established that the energy difference between the ground and spin-mixed intermediate states must be neither too small nor too large, with optimal values between 1 to 1.5 eV (so that optical transitions are facilitated but the spin-mixed intermediate states remain individually addressable[41]). A similar criterion holds for the energy difference between the initial and the final states: it should be neither too small (so that the two states are distinguishable) nor too big (otherwise the Λ process becomes inefficient and at the same time direct relaxation processes shorten the life-time of the energetically higher one). Here, an optimal value is around 1 cm^{-1} ($\approx 1.2 \times 10^{-4}$ eV). Therefore, the two almost degenerate ground states with opposite spin directions that originate from the same triplet state are the best choice. As for the intermediate states, they should be states in which a spin-up and a spin-down are mixed due to SOC, or the spin-switching process could be a spin forbidden process. This is a prerequisite for the spin-switching Λ processes.

Fig. 4(b) shows some of the lowest energy levels of the H-type Ni@B_{80} molecule with SOC and the transition information of the states involved in the spin dynamics. We select states $|1\rangle$ and $|3\rangle$ as the initial and final states, respectively, of a Λ process since they originate from the triplet ground state with opposite spin orientations and the splitting energy is about 0.058 eV, which fulfill the aforementioned energy requirement. The energy peaks of the optical spectrum in Fig. 4(c) propose some possible candidates for the initial intermediate states in the energy interval from 1.53 to 3.69 eV, which correspond to states $|7\rangle$, $|9\rangle$, $|13\rangle$, $|19\rangle$, $|21\rangle$, $|26\rangle$, $|37\rangle$, $|39\rangle$, $|55\rangle$ (shown as blue solid lines in Fig. 4(b)). Comparing the projected optical absorption spectra (Fig. 4(d)–(f)), we find that the oscillator strength along the *y* and *z* axes contribute most to the total oscillation spectra, while the oscillator strength along the *x* axis is very weak, which can be even neglected with respect to the oscillator strength along the *y* and *z* directions. In addition, the intense peaks in the *y*- and *z*-projected optical spectra are

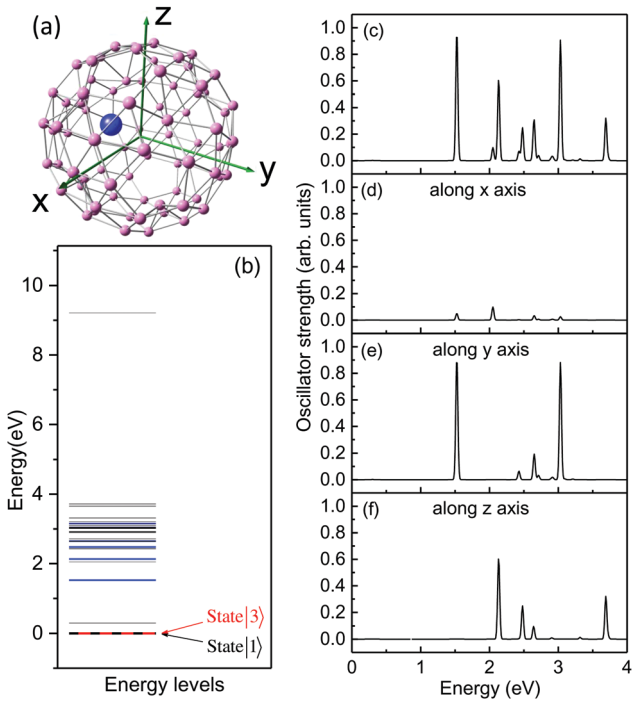

Fig. 4 (a) The optimized configuration of Ni@B_{80} in Cartesian coordinates. (b) The 61 lowest energy levels of Ni@B_{80} with SOC. The black dashed line represents state $|1\rangle$ and the red solid line denotes state $|3\rangle$. The blue solid lines represent 9 states that correspond to the peaks in the electronic optical spectra of state $|1\rangle$. (c) The calculated electronic optical absorption spectra in arbitrary units of state $|1\rangle$ (ground state) in the energy interval that contains the lowest 60 triplet states. (d)–(f) The projected optical spectra of state $|1\rangle$ along three different Cartesian axes. The horizontal axes in (c)–(f) denote the energy difference between excited state and ground state. (The states stemming from the same triplet term have almost identical spectra, therefore the spectra of state $|3\rangle$ are not shown here.)

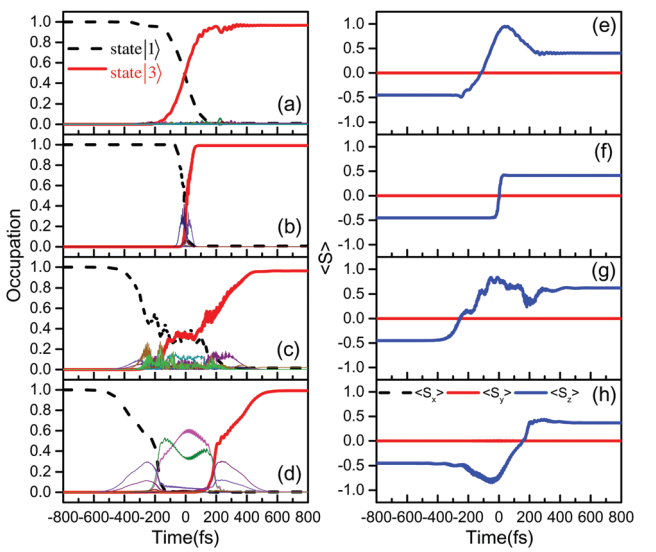

Fig. 5 The laser-induced spin switching (type A) on Ni@B_{80} *via* Λ processes. (a–d) Time evolution of the population of initial (dashed black), final (solid red) and intermediate (colorized solid) states. (e–h) Time-resolved expectation values of the spin components along three different Cartesian axes.

Table 3 Optimized laser parameters for each spin-switching scenario of Ni@B_{80} endohedral fullerene. θ and ϕ denote the angles of incidence in spherical coordinates, and γ is the angle between the polarization of light and the optical plane. FWHM is the full width at half maximum of the laser pulse

Process	Type	Fidelity	θ (°)	ϕ (°)	γ (°)	Intensity (J s^{-1} m^{-2})	FWHM (fs)	Energy (eV)
Λ_{12}	A	0.9664	181.58	258.30	226.28	1.048	299.7	2.410
	A*	0.9370	181.58	258.30	226.28	1.048	299.7	2.410
	B	0.9746	183.70	285.75	253.72	0.864	300.0	2.425
Λ_{19}	A	0.9920	259.00	19.00	46.10	0.053	50.0	1.982
	A*	0.9919	259.00	19.00	46.10	0.053	50.0	1.982
	B	0.9962	266.39	221.7	34.84	0.053	50.0	1.982
Λ_{25}	A	0.9636	183.70	204.81	202.35	0.720	300.0	3.178
	A*	0.9454	183.70	204.81	202.35	0.720	300.0	3.178
	B	0.9648	161.88	275.54	271.32	0.989	300.0	3.177
Λ_{37}	A	0.9923	117.54	17.24	308.97	1.051	300.0	3.635
	A*	0.9922	117.54	17.24	308.97	1.051	300.0	3.635
	B	0.9848	273.43	184.46	84.46	1.048	300.0	3.635

observed in different energy intervals (1.53 to 3.032 eV for the *y*-projected optical spectra, and 2.13 to 3.69 eV for the *z*-projected optical spectra). This phenomenon indicates that there could be more than one path for achieving the spin switching process and polarization orientation of the corresponding laser pulse. And finally, our genetic algorithm yields successful spin flip scenarios for the initial intermediate states $|12\rangle$, $|19\rangle$, $|25\rangle$, and $|37\rangle$, accounting for four different processes (for the sake of clarity, the corresponding switching processes are labeled as Λ_{12}, Λ_{19}, Λ_{25}, and Λ_{37}, respectively).

All the spin-switching processes can be achieved within the picosecond time regime and all population-transfer fidelities are larger than 0.95 (Fig. 5). Although the four achieved switching processes have the same initial and final states, the details of the population transfer processes are very different. For instance, it takes almost 1 ps for Λ_{37} to finish and 800 fs for Λ_{19} or Λ_{25}. Λ_{12} is by far the fastest, it completes within 100 fs. In addition, the $|1\rangle \rightarrow |3\rangle$ switch necessitates several Rabi-like cycles through processes Λ_{25} and Λ_{37}, while the other two processes are much smoother. The number of the involved intermediate states also varies with each process. What all processes have in common of course, is that they all originate from the combination of the time-dependent electric field of the laser pulses and SOC.[49]

In order to study the reversibility of each process we define three different spin-switching types: (i) a forward switching $|1\rangle \rightarrow |3\rangle$ using a laser pulse with parameters optimized by our genetic algorithm (type A); (ii) a backward switching from state $|3\rangle \rightarrow |1\rangle$ using exactly the same laser pulse as in type A without re-optimization (type A*); and (iii) a backward switching $|3\rangle \rightarrow |1\rangle$ using a laser pulse with parameters optimized by our genetic algorithm (type B). The high fidelities (about 95%, shown

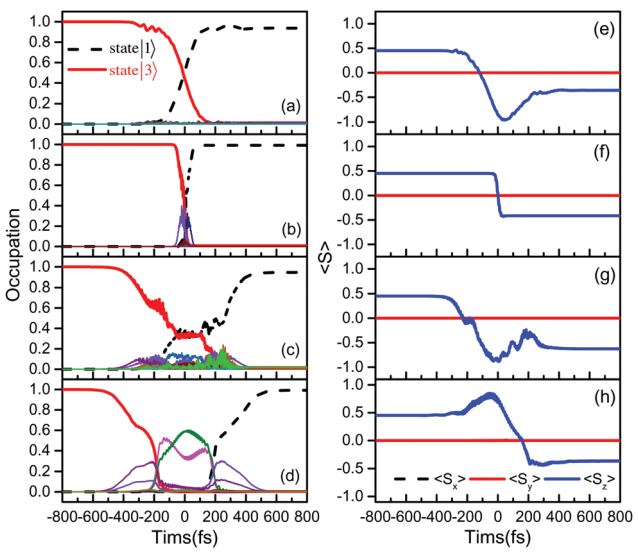

Fig. 6 The laser-induced spin switching (type A*) on Ni@B_{80} *via* Λ processes. (a–d) Time evolution of the population of initial (dashed black), final (solid red) and intermediate (colored solid) states. (e–h) Time-resolved expectation values of the spin components along three different Cartesian axes.

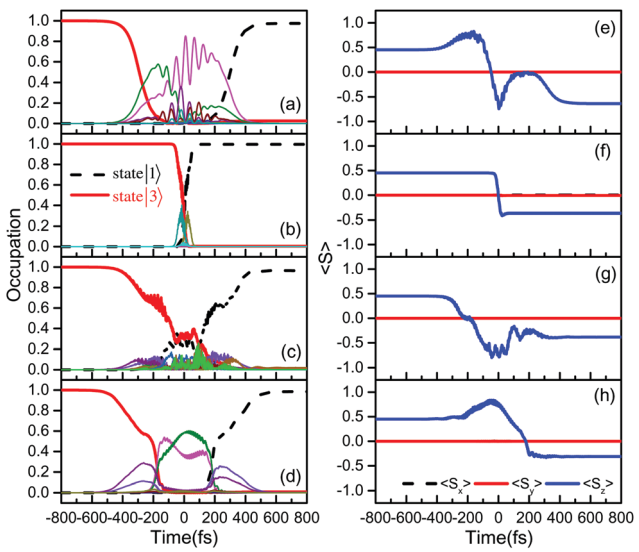

Fig. 7 The laser-induced spin switching (type B) on Ni@B_{80} *via* Λ processes. (a–d) Time evolution of the population of initial (dashed black), final (solid red) and intermediate (colored solid) states. (e–h) Time-resolved expectation values of the spin components along three different Cartesian axes.

Table 4 The intermediate states of spin-switching processes. E_{hs} denotes the energy of the highest intermediate state

Process	Type	Initial state	Final state	E_{hs} (eV)	Intermediate states
Λ_{12}	A	1	3	2.917	5,16,17,20,24,25,26,29,31,34
	A*	3	1		5,16,17,20,24,25,26,29,31,34
	B	3	1		5,16,17,20,24,25,26,29,31,34
Λ_{19}	A	1	3	2.479	10,11,13,15,18,19
	A*	3	1		10,11,13,15,18,19
	B	3	1		2,4,5,6,10,11,12,13,14,15,16,17,18,19
Λ_{25}	A	1	3	3.653	5,31,34,36,37,39,41,42,44,45,48,53
	A*	3	1		5,31,34,36,37,39,41,42,44,45,48,53
	B	3	1		5,31,34,36,37,39,41,42,44,45,48,53
Λ_{37}	A	1	3	3.726	5,49,50,53,55,57,59,60
	A*	3	1		5,49,50,53,55,57,59,60
	B	3	1		5,49,50,53,55,57,59,60

in Table 3) indicate the success of type-A* and type-B spin-switching processes, as well as for type-A processes.

Comparing Fig. 5 and 6, we observe that the population transfer in the two directions is almost perfectly symmetric and the intermediate states involved are the same for the types A and A*. As an example we mention that for Λ_{37}, both types A and A* proceed through states $|49\rangle$ and $|50\rangle$, which stem from the same triplet state (state 17) and split after SOC.

Generally, all type-A processes turn out to be reversible. In fact, the intermediate states are the same even for re-optimized pulses (type B), *i.e.*, states $|12\rangle$, $|19\rangle$, $|25\rangle$, and $|37\rangle$ (Fig. 7). It is also important that some processes start from an excited state (*e.g.*, $|3\rangle$), rather than the ground state $|1\rangle$. This is a desired feature, since we are aiming at magnetic nanologic devices which can also cope with the output of previous logic operations.

The detailed laser parameters involved in all the spin-switching processes are listed in Table 3. As a rule-of-thumb we can state that the intensity, energy, and full-width-at-half-maximum (FWHM) of the laser pulses do not display significant differences for the three types for the processes with the same initial intermediate state, with the exception of the direction of the incident light and the polarization angle. It is advantageous for the practical manipulation of the spin-switch process on H-type Ni@B_{80}, for which the laser-pulse requirements are not particularly strict (generally Λ processes exhibit a good tolerance with respect to the laser-pulse parameters[50,51]). Furthermore, the energy of the laser pulse varies for each process, allowing the logic functionalization of the H-type Ni@B_{80} with 8 different laser pulses, a flexibility which has never been seen in our previous investigations. It is also interesting that the energy of the laser pulse increases monotonically with the energy of the highest intermediate state (E_{hs}), as shown in Table 4.

4 Conclusions

In summary, we investigate the geometry and stability of the endohedral metallofullerene Ni@B_{80} using *ab initio* calculations. We also delve into its potential to be used as a magnetic nanologic device by studying laser-induced spin dynamics *via* Λ processes. The following conclusions can be drawn from our study:

(i) Three stable configurations of the endohedral metallofullerene Ni@B_{80} are theoretically predicted, in which the endohedral Ni atom is located (a) near the inner center of a hexagon (H type), (b) near the vertex of a pentagon (Pv type), or (c) near the midpoint of the common bond of two hexagons (HH type). Among them, the H-type structure is the most stable structure, has the highest spin density localized on the Ni atom and the least spin-polarized boron cage.

(ii) The spin-switching process on the endohedral metallofullerene Ni@B_{80} can be achieved through at least 8 different paths with different laser pulses. The fastest among them finishes in almost 100 fs.

(iii) All the spin processes on Ni@B_{80} proposed in the present work are reversible. In particular, the forward and reverse (backward) processes proceed in a highly symmetric manner, if the system is subjected to the same laser pulse, as long as the initial and final states originate from the same triplet state (after Zeeman and zero-field-splitting).

Acknowledgements

CL and JL acknowledge the National Natural Science Foundation (Grant No. 11572251 and 51210008) of China, the Program for New Century Excellent Talents in University of China (Grant No. NCET-12-0416), the Natural Science Basic Research Plan in Shaanxi Province of China (Grant No. 2014JQ1003), the Fundamental Research Funds for the Central Universities (Grant No. 3102014JCQ01043), and the Graduate Starting Seed Fund of NPU (Grant No. Z2016092). GL and WH acknowledge the German-Research-Foundation funded Transregional Collaborative Research Center SFB/TRR 88 ''3MET''.

References

1 E. Beaurepaire, J.-C. Merle, A. Daunois and J.-Y. Bigot, *Phys. Rev. Lett.*, 1996, **76**, 4250–4253.
2 C. Boeglin, E. Beaurepaire, V. Halté, V. Lopez-Flores, C. Stamm, N. Pontius, H. A. Duerr and J. Y. Bigot, *Nature*, 2010, **465**, 458–461.

3 B. Koopmans, J. Ruigrok, F. D. Longa and W. D. Jonge, *Phys. Rev. Lett.*, 2005, **95**, 267207.
4 S. Mangin, M. Gottwald, C. H. Lambert, D. Steil, V. Uhlir, L. Pang, M. Hehn, S. Alebrand, M. Cinchetti, G. Malinowski, Y. Fainman, M. Aeschlimann and E. E. Fullerton, *Nat. Mater.*, 2014, **13**, 286–292.
5 H. H. Guo, J. L. Liao, B. Ma, Z. Z. Zhang, Q. Y. Jin, H. Wang and J. P. Wang, *Appl. Phys. Lett.*, 2012, **100**, 142406.
6 U. Atxitia, O. Chubykalo-Fesenko, R. W. Chantrell, U. Nowak and A. Rebei, *Phys. Rev. Lett.*, 2009, **102**, 057203.
7 A. Sukhov and J. Berakdar, *Phys. Rev. Lett.*, 2009, **102**, 057204.
8 S. Saha, S. Barman, Y. Otani and A. Barman, *Nanoscale*, 2015, **7**, 18312–18319.
9 H. Shinohara, *Rep. Prog. Phys.*, 2000, **63**, 843–892.
10 A. A. Popov, S. Yang and L. Dunsch, *Chem. Rev.*, 2013, **113**, 5989–6113.
11 X. Lu, L. Feng, T. Akasaka and S. Nagase, *Chem. Soc. Rev.*, 2012, **41**, 7723–7760.
12 A. Fallah, Y. Yonetani, R. Senga, K. Hirahara, R. Kitaura, H. Shinohara and Y. Nakayama, *Nanoscale*, 2013, **5**, 11755–11760.
13 Q. Deng, T. Heine, S. Irle and A. A. Popov, *Nanoscale*, 2016, **8**, 3796–3808.
14 P. Moriarty, Y. R. Ma, M. D. Upward and P. H. Beton, *Surf. Sci.*, 1998, **407**, 27–35.
15 M. J. Butcher, F. H. Jonesl, P. Moriarty, P. H. Betonl, K. Prassides, K. Kordatos and N. Tagmatarchis, *Appl. Phys. Lett.*, 1999, **75**, 1074–1076.
16 S. C. Benjamin, A. Ardavan, G. A. D. Briggs, D. A. Britz, D. Gunlycke, J. Jefferson, M. A. G. Jones, D. F. Leigh, B. W. Lovett, A. N. Khlobystov, S. A. Lyon, J. J. L. Morton, K. Porfyrakis, M. R. Sambrook and A. M. Tyryshkin, *J. Phys.: Condens. Matter*, 2006, **18**, S867–S883.
17 W. Harneit, *Phys. Rev. A: At., Mol., Opt. Phys.*, 2002, **65**, 032322.
18 C. Ju, D. Suter and J. Du, *Phys. Lett. A*, 2011, **375**, 1441–1444.
19 C. Li, S. Zhang, W. Jin, G. Lefkidis and W. Hübner, *IEEE Trans. Magn.*, 2013, **49**, 3195–3198.
20 C. Li, J. Liu, S. Zhang, G. Lefkidis and W. Hübner, *Carbon*, 2015, **87**, 153.
21 N. G. Szwacki, A. Sadrzadeh and B. I. Yakobson, *Phys. Rev. Lett.*, 2007, **98**, 166804.
22 S. De, A. Willand, M. Amsler, P. Pochet, L. Genovese and S. Goedecker, *Phys. Rev. Lett.*, 2011, **106**, 225502.
23 T. Baruah, M. R. Pederson and R. R. Zope, *Phys. B*, 2008, **78**, 045408.
24 J. T. Wang, C. Chen, E. G. Wang, D. S. Wang, H. Mizuseki and Y. Kawazoe, *Appl. Phys. Lett.*, 2009, **94**, 133102.
25 J. L. Li and G. W. Yang, *Appl. Phys. Lett.*, 2009, **95**, 133115.
26 J. L. Li and G. W. Yang, *J. Phys. Chem. C*, 2009, **113**, 18292–18295.
27 N. G. Szwacki and C. J. Tymczak, *Chem. Phys. Lett.*, 2010, **494**, 80–83.
28 X. Q. Wang, *Phys. Rev. B: Condens. Matter Mater. Phys.*, 2010, **82**, 153409.
29 D. E. Bean, J. T. Muya, P. W. Fowler, M. T. Nguyen and A. Ceulemans, *Phys. Chem. Chem. Phys.*, 2011, **13**, 20855–20862.
30 W. Fa, S. Chen, S. Pande and X. C. Zeng, *J. Phys. Chem. A*, 2015, **119**, 11208–11214.
31 P. Pochet, L. Genovese, S. De, S. Goedecker, D. Caliste, S. A. Ghasemi, K. Bao and T. Deutsch, *Phys. Rev. B: Condens. Matter Mater. Phys.*, 2011, **83**, 081403.
32 H.-J. Zhai, Y.-F. Zhao, W.-L. Li, Q. Chen, H. Bai, H.-S. Hu, Z. A. Piazza, W.-J. Tian, H.-G. Lu, Y.-B. Wu, Y.-W. Mu, G.-F. Wei, Z.-P. Liu, J. Li, S.-D. Li and L.-S. Wang, *Nat. Chem.*, 2014, **6**, 727–731.
33 H. Bai, B. Bai, L. Zhang, W. Huang, Y.-W. Mu, H.-J. Zhai and S.-D. Li, *Sci. Rep.*, 2016, **6**, 35518.
34 Q. L. Lu, Q. Q. Luo, Y. D. Li and S. G. Huang, *Phys. Chem. Chem. Phys.*, 2015, **17**, 20897–20902.
35 Q. Chen, H.-R. Li, C.-Q. Miao, Y.-J. Wang, H.-G. Lu, Y.-W. Mu, G.-M. Ren, H.-J. Zhai and S.-D. Li, *Phys. Chem. Chem. Phys.*, 2016, **18**, 11610–11615.
36 Q. Chen, H.-R. Li, W.-J. Tian, H.-G. Lu, H.-J. Zhai and S.-D. Li, *Phys. Chem. Chem. Phys.*, 2016, **18**, 14186–14190.
37 H. Liu, *J. Nanjing Norm. Univ.*, 2003, **26**, 47.
38 M. J. Frisch, G. W. Trucks, H. B. Schlegel, G. E. Scuseria, M. A. Robb and J. R. Cheeseman, *GAUSSIAN 09, Revision A.1.*, Gaussian Inc., Wallingford, CT, 2009.
39 G. P. Zhang and W. Hübner, *Phys. Rev. Lett.*, 2000, **85**, 3025–3028.
40 G. Lefkidis and W. Hübner, *Phys. Rev. B: Condens. Matter Mater. Phys.*, 2007, **76**, 014418.
41 C. Li, W. Jin, H. Xiang, G. Lefkidis and W. Hübner, *Phys. Rev. B: Condens. Matter Mater. Phys.*, 2011, **84**, 054415.
42 W. Jin, F. Rupp, K. Chevalier, M. M. N. Wolf, M. C. Rojas, G. Lefkidis, H. J. Krüger, R. Diller and W. Hübner, *Phys. Rev. Lett.*, 2012, **109**, 267209.
43 G. Lefkidis, C. Li, G. Pal, M. Blug, H. Kelm, H. J. Kruger and W. Hübner, *J. Phys. Chem. A*, 2011, **115**, 1774–1780.
44 C. Li, S. Zhang, W. Jin, H. Xiang, G. Lefkidis and W. Hübner, *J. Magn. Magn. Mater.*, 2012, **324**, 4024–4029.
45 P. J. Hay and W. R. Wadt, *J. Chem. Phys.*, 1985, **82**, 299–310.
46 C. Li, S. Zhang, W. Jin, G. Lefkidis and W. Hübner, *Phys. Rev. B: Condens. Matter Mater. Phys.*, 2014, **89**, 184404.
47 H. Nakatsuji, *Chem. Phys. Lett.*, 1979, **67**, 329–333.
48 T. Hartenstein, C. Li, G. Lefkidis and W. Hübner, *J. Phys. D: Appl. Phys.*, 2008, **41**, 180413.
49 W. Töws and G. Pastor, *Phys. Rev. Lett.*, 2015, **115**, 217204.
50 D. Chaudhuri, W. Jin, G. Lefkidis and W. Hübner, *J. Chem. Phys.*, 2015, **143**, 174303.
51 W. Jin, M. Becherer, D. Bellaire, G. Lefkidis, M. Gerhards and W. Hübner, *Phys. Rev. B: Condens. Matter Mater. Phys.*, 2014, **89**, 144409.